Editors' Suggestion | Featured in Physics

Emergent Dirac Gullies and Gully-Symmetry-Breaking Quantum Hall States in *ABA* Trilayer Graphene

A. A. Zibrov,[1] P. Rao,[2] C. Kometter,[1] E. M. Spanton,[3] J. I. A. Li,[4] Cory R. Dean,[4] T. Taniguchi,[5] K. Watanabe,[5] M. Serbyn,[2] and A. F. Young[1]

[1]*Department of Physics, University of California, Santa Barbara, California 93106, USA*
[2]*Institute of Science and Technology, Am Campus 1, 3400 Klosterneuburg, Austria*
[3]*California Nanosystems Institute, University of California, Santa Barbara, California 93106, USA*
[4]*Department of Physics, Columbia University, New York, New York 10025, USA*
[5]*Advanced Materials Laboratory, National Institute for Materials Science, Tsukuba, Ibaraki 305-0044, Japan*

(Received 27 April 2018; published 15 October 2018)

We report on quantum capacitance measurements of high quality, graphite and hexagonal boron nitride encapsulated Bernal stacked trilayer graphene devices. At zero applied magnetic field, we observe a number of electron density- and electrical displacement-tuned features in the electronic compressibility associated with changes in Fermi surface topology. At a high displacement field and low density, strong trigonal warping gives rise to three new emergent Dirac cones in each valley, which we term "gullies." The gullies are centered around the corners of a hexagonal Brillouin zone and related by threefold rotation symmetry. At low magnetic fields of $B = 1.25$ T, the gullies manifest as a change in the degeneracy of the Landau levels from two to three. Weak incompressible states are also observed at integer filling within these triplet Landau levels, which a Hartree-Fock analysis indicates are associated with Coulomb-driven nematic phases that spontaneously break rotation symmetry.

DOI: 10.1103/PhysRevLett.121.167601

In graphene multilayers, strong trigonal warping of the electronic band structure leads to a complex evolution of Fermi surface topology within the low energy valleys located at the corners of the hexagonal Brillouin zone [1,2]. The comparatively small energy scales characterizing the underlying interlayer hopping processes (∼100 meV) renders these transitions accessible via electrostatic gating, providing a highly tunable platform for engineering both zero and high magnetic field electronic structure. Of particular interest is the possibility of using band structure engineering to create novel manifolds of degenerate Landau levels (LLs), where enhanced electron-electron interaction effects can lead to novel correlated ground states. However, such control comes at the cost of requiring high sample quality to avoid smearing the subtle electronic features.

In this Letter, we report magnetocapacitance measurements of exceptionally high quality Bernal-stacked (*ABA*) trilayer graphene (TLG) devices [Fig. 1(a)]. Absent an applied perpendicular electric field, the band structure of *ABA* TLG is described by independent linear and parabolic bands [3–5] resembling those found in monolayer graphene (MLG) and bilayer graphene (BLG), respectively, in each of the two valleys centered at the high symmetry K and K' points [Fig. 1(b)]. An applied electric displacement field $\vec{D}$ strongly hybridizes these two sectors, driving the linear monolayerlike band to high energies and generating new structure in the low-energy bilayerlike bands [Fig. 1(c)]. For large electric fields, the strong trigonal warping is predicted to lead to the formation of new Dirac gullies centered around each of the two original valleys [6,7] and are related to each other by threefold rotation symmetry. At quantizing magnetic fields, the threefold symmetry of the gullies may lead to novel broken symmetry ground states [8], including nematic states as recently observed on the surface of high purity bismuth crystals [9].

Past experiments on *ABA* trilayer graphene [10–19] have observed features associated with numerous aspects of the single particle band structure, including a variety of electric- and magnetic-field tuned LL crossings [20,21] that tightly constrain band structure parameters [13,16]. Recent experiments have also found evidence for interaction-induced quantum Hall ferromagnetic states at high magnetic field [15,18,19]. However, the high-electric field regime of the Dirac gullies has not been explored in high mobility devices where interaction driven states might be accessible.

To access the high mobility, high-D regime, we study *ABA* trilayer flakes encapsulated in hexagonal boron nitride (BN) dielectric layers and single-crystal graphite gates [22] [Fig. 1(d)]. We use few-layer graphite to contact the trilayer, allowing us to vary both the total charge density and displacement field $\vec{D}$ across the trilayer [Fig. 1(e)]. We measure the penetration field capacitance C_P [23], defined as the capacitance between the top and bottom gate with the graphene layer held at constant potential. The finite density of states $\partial n/\partial \mu$ of the trilayer partially screens the electric

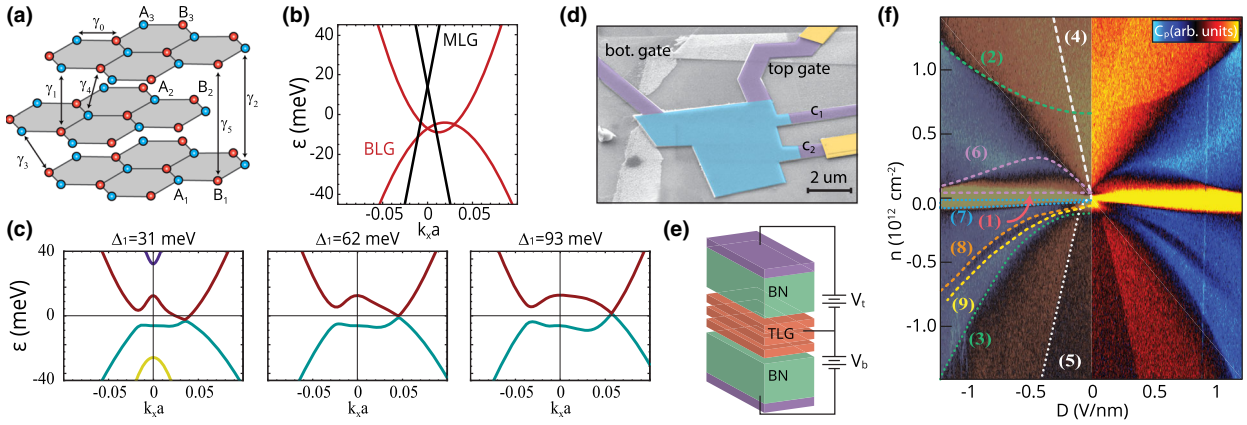

FIG. 1. Trilayer graphene band structure and penetration field capacitance measurements at $B = 0$. (a) Lattice structure of ABA trilayer graphene with hopping parameters identified. In addition to the γ_i, the electronic structure is determined by the interlayer potentials $\Delta_1 \propto D$ and the relative potential of the inner layer with respect to the outer layers, Δ_2. (b) Electronic band structure of trilayer graphene in the absence of an applied displacement field. The linear monolayerlike and parabolic bilayerlike bands are labeled. The momentum is relative to the K point in the $\vec{k}_x \| \Gamma - K$ direction. (c) Band structure evolution under applied electric field. For a wide range of electric fields, the low energy structure is described by three isolated Dirac cones slightly displaced from the $K(K')$ points. (d) False color electron micrograph of the measured trilayer graphene device. The active region is indicated in cyan. (e) Device schematic: trilayer graphene encapsulated in ~20 nm BN with few-layer graphite top and bottom gates. Independent contacts to the gates and graphene layer allow independent control of charge density $n = c_t V_t + c_b V_b$ and displacement electric field $D = \epsilon_{\mathrm{BN}}(V_t/d_t - V_b/d_b)$, where $\epsilon_{\mathrm{BN}} \approx 3$ and $d_{t(b)} = 18$, 20 nm are the distances to the gates. (f) Penetration field capacitance C_P at $B = 0$ T and $T \approx 50$ mK as a function of n and D. D breaks the mirror symmetry of the ABA-stacked trilayer graphene and induces an on-site energy difference Δ_1 between the outer layers. Main features visible in the experimental data are indicated by dashed lines and numerals. The $D < 0$ region is shaded to increase the visibility of the features. Data are plotted on a saturated color scale (see Fig. S5).

field between the top and bottom gate, reducing the measured C_P so that (for top and bottom gates with geometric capacitance c) $C_P = c^2/(2c + \partial n/\partial\mu) \propto (\partial n/\partial\mu)^{-1}$ for $\partial n/\partial\mu \gg c$. Thus, changes in C_P are associated with changes in the Fermi surface size or topology.

Figure 1(f) shows C_P measured at $B = 0$ as a function of D and electron density n. A variety of n and D-tuned discontinuities are readily visible and indicated in the figure with numeric labels (1)–(9). These include a sharp C_P maximum at charge neutrality for both positive and negative D (1), two elevated C_P features with parabolic boundaries at negative and positive n (2)–(3), two low-C_P regions with triangular boundary within the parabolic regions (4)–(5), a "wing-shaped" high C_P region both above and below charge neutrality (6)–(7), and a narrow elevated C_P region that runs parallel to the parabolic feature for negative n bounded by contours (8)–(9). Some of the capacitance features can be associated with the single-particle band structure by inspection. For example, (1) is consistent with the small band gap or linear band crossing expected at charge neutrality [6]. Features (4)–(5), meanwhile, are identified as the extrema of the linear bands [purple and yellow in Fig. 1(c)] which disperse rapidly to high energy with increasing D. Thus, additional features are associated with the complex band minima of the low energy bands.

To understand the remaining observed compressibility features, we perform tight binding simulations of the trilayer graphene band structure. Energy eigenvalues are computed using a six-band tight binding model (see Supplemental Material [24]). Hopping between different atoms within the unit cell is parametrized by six tight binding parameters γ_i, $i = 1, \ldots, 6$, one on-site energy δ, and two energy asymmetries Δ_1 and Δ_2. Δ_1 describes the potential difference between the top and bottom layers and is most directly tuned by the strength of an externally applied polarizing electric field D. Δ_2 measures the potential imbalance between the central layer and the two outer layers and screening effects within the trilayer.

Figure 2(a) shows the calculated inverse compressibility within this model, as a function of the carrier density and $\Delta_1 \propto |\vec{D}|$. Both the geometric and parasitic capacitances within the device influence the mapping of $\partial n/\partial\mu \leftrightarrow C_P$ between calculated compressibility and measured data. Moreover, interactions likely renormalize the compressibility particularly when it is high. Thus, we restrict ourselves to qualitative comparisons of the magnitude of the signals and plot both in arbitrary units. We do, however, achieve quantitative agreement between data and simulation for the position of extrema and discontinuities for parameters $\gamma_0 = 3.1, \gamma_1 = .38, \gamma_2 = -0.021(5), \gamma_3 = 0.29, \gamma_4 = 0.141(40), \gamma_5 = 0.050(5), \delta = 0.0355(45)$, and $\Delta_2 = 0.0035$, where all energies are expressed in eV. Notably, the model succeeds in matching the experimentally observed features only for an exceptionally narrow range of parameters, providing tighter constraints on $\{\gamma_i\}$ and $\{\Delta_i\}$ than previously achieved using only LL

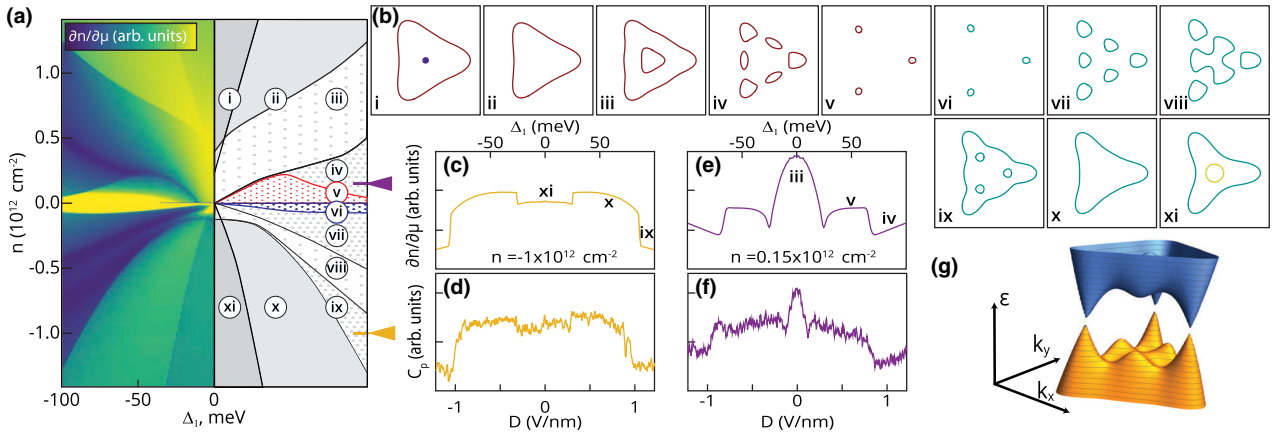

FIG. 2. Fermi surface topology (a) Left: Inverse electronic compressibility $\partial n/\partial\mu$ calculated from a six-band tight binding Hamiltonian as a function of interlayer asymmetry Δ_1 and electron density n. Right: schematic showing regions (indexed by the Roman numerals) separated by sharp changes in the compressibility. (b) Fermi contours calculated at each of the points indexed by roman numerals in (a). Color indicates the band and follows the convention of Fig. 1(c); note that panels (i)–(v) are Fermi surfaces of electrons while (vi)–(xi) are Fermi surfaces of holes. (c) Simulated $\partial n/\partial\mu$ and (d) measured C_P at $n = -1 \times 10^{12}$ cm^{-2}. The discontinuous jump in the data at $D \approx \pm.3$ V/nm coincides with population of the second hole subband [(xi)–(x) transition], while the jump at $D \approx \pm.95$ V/nm coincides with the opening of internal electronlike Fermi surfaces within the main hole pocket [(x)–(ix) transition]. (e) Simulated $\partial n/\partial\mu$ and (f) measured C_P at $n = .15 \times 10^{12}$ cm^{-2}. The sharp minimum at $D \approx \pm.5$ V/nm coincides with a Lifshitz transition from one multiply connected electron pocket [(iii)] to three disconnected Dirac cones [(v)]. At the discontinuity at $D \approx \pm.9$ V/nm, the Dirac cones are joined by three additional auxiliary pockets. (g) Band structure near K point for $\Delta_1 = 75$ meV showing the emergent Dirac gullies.

coincidences [13,17,33]. In addition to the parameters γ_i and Δ_2, a single scale factor $\alpha = .165e$ nm is chosen so that $\Delta_1 = \alpha D$. α describes dielectric screening of the perpendicular electric field by the trilayer, implying an effective $\epsilon^{\perp}_{\mathrm{TLG}} \approx 4$ for the trilayer itself (see Supplemental Material [24]).

The agreement between theory and experiment allows us to understand the connection between the observed compressibility features and the nature of the Fermi contours. Figure 2(b) shows calculated Fermi surface contours in 11 distinct regions throughout the experimentally accessed parameter regime. Regions (i) and (xi), e.g., are distinguished by the existence of a second, independent Fermi surface arising from the second electron- or hole-subband, respectively, as intuited above. All other regions are separated by Lifshitz transitions and distinguished by differences in Fermi surface topology within a single electron- or hole-band. We note that signatures of Lifshitz transitions were recently found in tetralayer graphene [2] at zero magnetic field, but no direct compressibility measurements of Lifshitz transitions have been reported. With the exception of regions (iii)–(iv), all of the regions are bounded by experimentally observed features described in Fig. 1. We note that features characterized by a diverging density of states, such as the (iii)–(iv) boundary, only weakly modify the measured capacitance and are barely discernible even in Fig. 1(f).

Figures 2(c)–2(d) show comparisons of traces from the measured capacitance and the numerically calculated inverse compressibility at $n = -1.0 \times 10^{12}$ cm^{-2}. Both data and simulation show matching discontinuities associated with the band edge of the second hole subband [i.e., the (xi)–(x) transition] as well as the nucleation of three new electron pockets within the main holelike Fermi pocket (x)–(ix). Of particular interest is the regime of low n and large D, where the gully Dirac points are predicted [6]. Figures 2(e)–2(f) show line traces at $n = .15 \times 10^{12}$ cm^{-2}. The wing region, bounded by sharp discontinuities in both the measured signal and simulated data, is readily identified with region v, in which the Fermi surface arises from three isolated gully Dirac cones [Fig. 2(g)].

In addition to its thermodynamic signatures at $B = 0$, the emergence of isolated Dirac cones can be expected to lead to new transport, optical, and thermodynamic phenomenology at finite magnetic fields. In monolayer graphene, e.g., the two inequivalent valleys lead to fourfold internal degeneracy of the LLs, with an additional factor of 2 arising from electron spin. The observation of fourfold degeneracy was a critical feature of the first experimental demonstrations of the Dirac spectrum in monolayer graphene [34,35].

The gully Dirac cones similarly manifest as increased LL degeneracy. Figure 3(a) shows C_P data measured at $B = 1.25$ T alongside the results of diagonalizing the trilayer Hamiltonian in the presence of a magnetic field (simulations ignore spin splitting; see Supplemental Material [24]). Larger energy gaps manifest as prominent peaks in C_P at filling factors $\nu = eBn/h$, spaced by integer multiples of g, the internal LL degeneracy. Near $D = 0$,

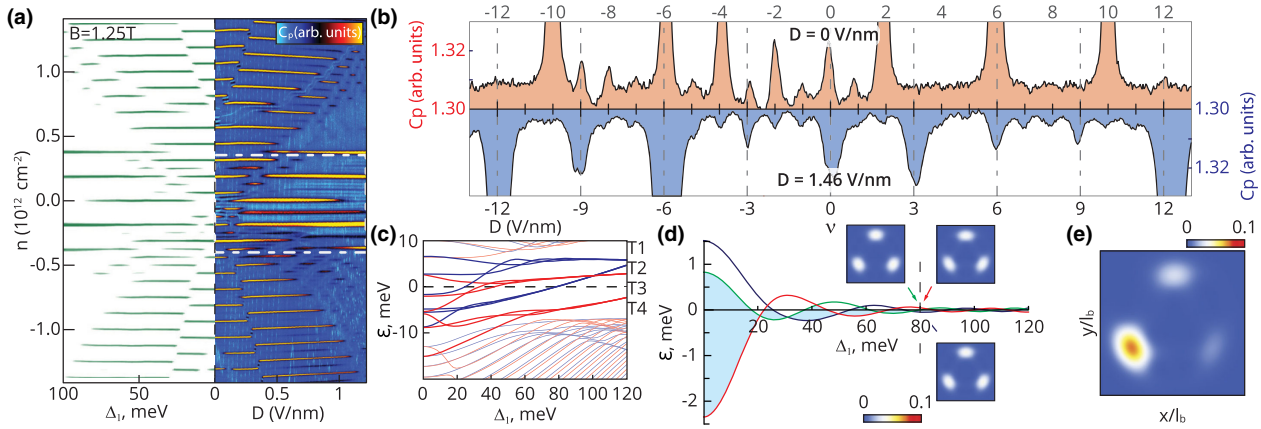

FIG. 3. Triplet Landau levels and interaction induced symmetry breaking. (a) Right panel: Penetration field capacitance C_P measured at $B = 1.25$ T as a function of D and n. The dashed lines indicate the region of low carrier density near the valence and conduction band minima where trigonal warping has the strongest effect and leads to a formation of new Dirac points. Left panel: simulated inverse compressibility at $B = 1.25$ T based on band structure parameters. A phenomenological thermal broadening of 0.1 meV is assumed to generate contrast, so that only the largest gaps are visible in green. (b) C_P traces for $n \in [-0.5, 0.5] \times 10^{12}$ cm^{-2} at $D = 0$ (red) and at $D = 1.46$ V/nm (blue). The $D = 0$ line trace shows strong capacitance peaks at even filling factors, in contrast to the peaks at multiples of three ($\nu = \pm 3, 6, 9, 12$) for $D = 1.46$ V/nm. (c) Evolution of LLs at $B = 1.25$ T as a function of interlayer potential difference Δ_1. As the electric potential increases, 12 distinct LLs at $\Delta_1 \approx 0$ intertwine into four quasidegenerate triplets, denoted $T_1, \ldots, T_4$, separated from a near- continuum of closely spaced LLs by energy gaps. (d) Expanded view of the triplet $T2$ with the average energy of the triplet subtracted. Insets show the real-space probability distribution for a coherent state formed from functions in each of the component LLs. All respect rotation symmetry. (e) Real-space probability distribution of the Hartree-Fock ground state at 1/3 filling of the spin-polarized triplet $T2$ at $\Delta_1 = 80$ meV, showing strongly broken threefold rotation symmetry.

we observe the strongest capacitance peaks spaced by $\Delta\nu = 2$, in agreement with the twofold valley degeneracy ($g = 2$) but lifted spin degeneracy [Fig. 3(b), top]. In contrast, at large displacement fields ($D > 0.7$ V/nm) and near charge neutrality—i.e., in the regime of the Dirac gullies—this behavior changes, with the most prominent gaps spaced by $\Delta\nu = 3$ for $-12 < \nu < 12$ [see Fig. 3(b), bottom]. The calculated single particle energy spectrum [Fig 3(c)] shows that displacement field leads to the formation of four triplets of LLs per spin projection (labeled $T1$, $T2$, $T3$, and $T4$); within each triplet, three LLs intertwine into a single threefold quasidegenerate band consistent with the observed LL degeneracy. We note that triplet LLs are a generic feature of trigonally warped multilayer band structures, and evidence for threefold degenerate LLs has previously been reported in suspended bilayer graphene samples [36].

While the observation of triplet LLs is consistent with expectations from our single-particle model, close examination of high D data reveals departures from the noninteracting picture. In particular, we observe C_P peaks at all integer filling factors $-6 < \nu < 12$, corresponding to the dashed region of Fig. 3(a) (see, also, Fig. S6), including weak peaks at (ν mod 3) $\neq 0$. These gaps persist without closing over the whole range of $D > 0.7$ V/nm. This is qualitatively inconsistent with the single particle spectrum, which predicts that, within each triplet [$T1, \ldots, T4$ in Fig. 3(c)], the single particle eigenstates evolve via a series of crossings with increasing Δ_1 [Fig. 3(d)]. Thus, one expects these anomalous gaps to undergo repeated closings, in contrast to their observed persistence.

The failure of the single-particle picture is not surprising. The estimated bandwidth of each triplet [Fig. 3(d)], $\delta\varepsilon < 0.5$ meV, is smaller than the scale of the Coulomb interactions, $E_C = e^2/(\epsilon \ell_B) \approx 10$ meV at $B = 1.25$ T [here e is the elementary charge, $\epsilon = 6.6$ the in-plane dielectric constant of BN [37], and $\ell_B = \sqrt{\hbar/(eB)}$ the magnetic length]. Taking these interactions into account, the individual LLs within the triplet are effectively degenerate; the ground state at integer filling must result from minimizing repulsive interactions and is likely to result in a gapped, symmetry breaking quantum Hall ferromagnetic state.

We investigate this quantitatively using a variational Hartree-Fock analysis (see Supplemental Material [24]) of the ground state when only one out of three LLs within a single spin branch of triplet $T2$ is filled (1/3 filling). The three insets to Fig. 3(d) show real space probability distributions for coherent states constructed for each of the three components of $T2$. Absent interactions, the ground state at 1/3 filling consists of the lower energy component of $T2$ for a given value of B and Δ_1, and preserves rotation symmetry. In contrast, the Hartree-Fock ground state [Fig. 3(e)] spontaneously breaks the C_3 symmetry—it is a gully nematic. As long as $\delta\varepsilon \ll E_C$, the gap will be only weakly modulated by Δ_1, making it insensitive to the single-particle level crossings, in agreement with experimental observation.

The nematic ground state is merely one example of a symmetry breaking channel. Intuitively, nematics are favored by interactions when LL wave functions are localized in well separated real-space pockets, as in the case in the highly anisotropic wave functions of Fig. 3(e). In a momentum space picture, these pockets are associated with the main Dirac gullies represented in the contours of Fig. 2(b) (v)–(vi). In this limit, *ABA* trilayer triplet LLs resemble the case of the (111) surface of SnTe recently considered theoretically [38]. Our single-particle calculations suggest that other limiting behaviors can also be realized in *ABA* trilayer graphene, resulting in qualitatively different ground states. For instance, the triplet states $T1$ and $T4$ are considerably less anisotropic, being associated with multiple momentum space pockets close to the $K(K')$ points as in Fig 2(b) (vii). In these triplets, isotropic ground states constructed from a superposition of triplet wave functions may be favored. Notably, the relevant anisotropies within each triplet are continuously tunable by external electric and magnetic fields, making *ABA* trilayer graphene a remarkably versatile platform for exploring correlation effects in unusual quantum Hall ferromagnets. Cataloging the theoretical possibilities and determining how to distinguish them experimentally will be the topic of future work.

The experimental work at UCSB was funded by the National Science Foundation under Grant No. DMR-1654186. Work at Columbia was supported by the National Science Foundation under Grant No. DMR-1507788. K. W. and T. T. acknowledge support from the Elemental Strategy Initiative conducted by the Ministry of Education, Culture, Sports, Science and Technology, Japan, and the Japan Society for the Promotion of Science KAKENHI Grant No. JP15K21722. E. M. S. acknowledges the support of the Elings Fellowship from the California Nanosystems Institute at the University of California, Santa Barbara. A. F. Y. acknowledges the support of the David and Lucile Packard foundation and the Sloan Foundation. Measurements made use of a dilution refrigerator funded through the Major Research Instrumentation program of the U.S. National Science Foundation under Grant No. DMR-1531389, and the MRL Shared Experimental Facilities, which are supported by the MRSEC Program of the U.S. National Science Foundation under Grant No. DMR-1720256.

[1] E. McCann and V. I. Fal'ko, Landau-Level Degeneracy and Quantum Hall Effect in a Graphite Bilayer, Phys. Rev. Lett. **96**, 086805 (2006).

[2] Y. Shi, S. Che, K. Zhou, S. Ge, Z. Pi, T. Espiritu, T. Taniguchi, K. Watanabe, Y. Barlas, R. Lake, and C. N. Lau, Tunable Lifshitz Transitions and Multiband Transport in Tetralayer Graphene, Phys. Rev. Lett. **120**, 096802 (2018).

[3] M. Koshino and E. McCann, Gate-induced interlayer asymmetry in *ABA*-stacked trilayer graphene, Phys. Rev. B **79**, 125443 (2009).

[4] B. Partoens and F. M. Peeters, From graphene to graphite: Electronic structure around the K point, Phys. Rev. B **74**, 075404 (2006).

[5] A. A. Avetisyan, B. Partoens, and F. M. Peeters, Electric-field control of the band gap and Fermi energy in graphene multilayers by top and back gates, Phys. Rev. B **80**, 195401 (2009).

[6] M. Serbyn and D. A. Abanin, New Dirac points and multiple Landau level crossings in biased trilayer graphene, Phys. Rev. B **87**, 115422 (2013).

[7] T. Morimoto and M. Koshino, Gate-induced Dirac cones in multilayer graphenes, Phys. Rev. B **87**, 085424 (2013).

[8] I. Sodemann, Z. Zhu, and L. Fu, Quantum Hall Ferroelectrics and Nematics in Multivalley Systems, Phys. Rev. X **7**, 041068 (2017).

[9] B. E. Feldman, M. T. Randeria, A. Gyenis, F. Wu, H. Ji, R. J. Cava, A. H. MacDonald, and A. Yazdani, Observation of a nematic quantum Hall liquid on the surface of bismuth, Science **354**, 316 (2016).

[10] M. F. Craciun, S. Russo, M. Yamamoto, J. B. Oostinga, A. F. Morpurgo, and S. Tarucha, Trilayer graphene is a semimetal with a gate-tunable band overlap, Nat. Nanotechnol. **4**, 383 (2009).

[11] A. Kumar, W. Escoffier, J. M. Poumirol, C. Faugeras, D. P. Arovas, M. M. Fogler, F. Guinea, S. Roche, M. Goiran, and B. Raquet, Integer Quantum Hall Effect in Trilayer Graphene, Phys. Rev. Lett. **107**, 126806 (2011).

[12] E. A. Henriksen, D. Nandi, and J. P. Eisenstein, Quantum Hall Effect and Semimetallic Behavior of Dual-Gated *ABA*-Stacked Trilayer Graphene, Phys. Rev. X **2**, 011004 (2012).

[13] T. Taychatanapat, K. Watanabe, T. Taniguchi, and P. Jarillo-Herrero, Quantum Hall effect and Landau-level crossing of Dirac fermions in trilayer graphene, Nat. Phys. **7**, 621 (2011).

[14] W. Bao, L. Jing, J. Velasco, Y. Lee, G. Liu, D. Tran, B. Standley, M. Aykol, S. B. Cronin, D. Smirnov, M. Koshino, E. McCann, M. Bockrath, and C. N. Lau, Stacking-dependent band gap and quantum transport in trilayer graphene, Nat. Phys. **7**, 948 (2011).

[15] Y. Lee, J. Velasco, D. Tran, F. Zhang, W. Bao, L. Jing, K. Myhro, D. Smirnov, and C. N. Lau, Broken symmetry quantum Hall states in dual-gated *ABA* trilayer graphene, Nano Lett. **13**, 1627 (2013).

[16] L. C. Campos, A. F. Young, K. Surakitbovorn, K. Watanabe, T. Taniguchi, and P. Jarillo-Herrero, Quantum and classical confinement of resonant states in a trilayer graphene Fabry-Pérot interferometer, Nat. Commun. **3**, 1239 (2012).

[17] Y. Shimazaki, T. Yoshizawa, I. V. Borzenets, K. Wang, X. Liu, K. Watanabe, T. Taniguchi, P. Kim, M. Yamamoto, and S. Tarucha, Landau level evolution driven by band hybridization in mirror symmetry broken *ABA*-stacked trilayer graphene., arXiv:1611.02395.

[18] P. Stepanov, Y. Barlas, T. Espiritu, S. Che, K. Watanabe, T. Taniguchi, D. Smirnov, and C. N. Lau, Tunable Symmetries of Integer and Fractional Quantum Hall Phases in Heterostructures with Multiple Dirac Bands, Phys. Rev. Lett. **117**, 076807 (2016).

[19] B. Datta, S. Dey, A. Samanta, H. Agarwal, A. Borah, K. Watanabe, T. Taniguchi, R. Sensarma, and M. M. Deshmukh, Strong electronic interaction and multiple quantum Hall ferromagnetic phases in trilayer graphene, Nat. Commun. **8**, 14518 (2017).

[20] M. Koshino and E. McCann, Landau level spectra and the quantum Hall effect of multilayer graphene, Phys. Rev. B **83**, 165443 (2011).

[21] S. Yuan, R. Roldán, and M. I. Katsnelson, Landau level spectrum of *ABA*- and *ABC*-stacked trilayer graphene, Phys. Rev. B **84**, 125455 (2011).

[22] A. A. Zibrov, C. Kometter, H. Zhou, E. M. Spanton, T. Taniguchi, K. Watanabe, M. P. Zaletel, and A. F. Young, Tunable interacting composite fermion phases in a half-filled bilayer-graphene Landau level, Nature (London) **549**, 360 (2017).

[23] J. P. Eisenstein, L. N. Pfeiffer, and K. W. West, Negative Compressibility of Interacting Two-Dimensional Electron and Quasiparticle Gases, Phys. Rev. Lett. **68**, 674 (1992).

[24] See Supplemental Material at http://link.aps.org/supplemental/10.1103/PhysRevLett.121.167601 for additional data and theoretical simulations, which includes Refs. [25–32].

[25] M. S. Dresselhaus and G. Dresselhaus, Intercalation compounds of graphite, Adv. Phys. **51**, 1 (2002).

[26] C. L. Lu, C. P. Chang, Y. C. Huang, R. B. Chen, and M. L. Lin, Influence of an electric field on the optical properties of few-layer graphene with *AB* stacking, Phys. Rev. B **73**, 144427 (2006).

[27] F. Guinea, A. H. C. Neto, and N. M. R. Peres, Electronic states and Landau levels in graphene stacks, Phys. Rev. B **73**, 245426 (2006).

[28] H. Min, B. Sahu, S. K. Banerjee, and A. H. MacDonald, *Ab initio* theory of gate induced gaps in graphene bilayers, Phys. Rev. B **75**, 155115 (2007).

[29] A. Grüneis, C. Attaccalite, L. Wirtz, H. Shiozawa, R. Saito, T. Pichler, and A. Rubio, Tight-binding description of the quasiparticle dispersion of graphite and few-layer graphene, Phys. Rev. B **78**, 205425 (2008).

[30] B. Datta, H. Agarwal, A. Samanta, A. Ratnakar, K. Watanabe, T. Taniguchi, R. Sensarma, and M. M. Deshmukh, Landau Level Diagram and the Continuous Rotational Symmetry Breaking in Trilayer Graphene, Phys. Rev. Lett. **121**, 056801 (2018).

[31] A. H. MacDonald, Influence of Landau-level mixing on the charge-density-wave state of a two-dimensional electron gas in a strong magnetic field, Phys. Rev. B **30**, 4392 (1984).

[32] F. Zhang, D. Tilahun, and A. H. MacDonald, Hund's rules for the $N = 0$ Landau levels of trilayer graphene, Phys. Rev. B **85**, 165139 (2012).

[33] L. C. Campos, T. Taychatanapat, M. Serbyn, K. Surakitbovorn, K. Watanabe, T. Taniguchi, D. A. Abanin, and P. Jarillo-Herrero, Landau Level Splittings, Phase Transitions, and Nonuniform Charge Distribution in Trilayer Graphene, Phys. Rev. Lett. **117**, 066601 (2016).

[34] Y. Zhang, Y.-W. Tan, H. L. Stormer, and P. Kim, Experimental observation of the quantum Hall effect and Berry's phase in graphene, Nature (London) **438**, 201 (2005).

[35] K. S. Novoselov, A. K. Geim, S. V. Morozov, D. Jiang, M. I. Katsnelson, I. V. Grigorieva, S. V. Dubonos, and A. A. Firsov, Two-dimensional gas of massless Dirac fermions in graphene, Nature (London) **438**, 197 (2005).

[36] A. Varlet, D. Bischoff, P. Simonet, K. Watanabe, T. Taniguchi, T. Ihn, K. Ensslin, M. Mucha-Kruczyński, and V. I. Fal'ko, Anomalous Sequence of Quantum Hall Liquids Revealing a Tunable Lifshitz Transition in Bilayer Graphene, Phys. Rev. Lett. **113**, 116602 (2014).

[37] R. Geick, C. H. Perry, and G. Rupprecht, Normal modes in hexagonal boron nitride, Phys. Rev. **146**, 543 (1966).

[38] X. Li, F. Zhang, and A. H. MacDonald, SU(3) Quantum Hall Ferromagnetism in SnTe, Phys. Rev. Lett. **116**, 026803 (2016).